

# A Mixed-Field Formulation for Modeling Dielectric Ring Resonators and its Application in Optical Frequency Comb Generation

Ergun Simsek, Alioune Niang, Raonaqul Islam, Logan Courtright,  
Gary Carter, and Curtis R. Menyuk

June 23, 2025

## Abstract

We present a novel finite-difference frequency-domain formulation for accurate and efficient modal analysis of dielectric ring resonators, a critical component in microresonator-based optical frequency comb (OFC) generation. Unlike previous methods, our approach solves for both electric and magnetic fields simultaneously in cylindrical coordinates, eliminating spurious modes and ensuring high fidelity at material boundaries. The solver enables rapid computation of resonant modes without requiring manual input for azimuthal mode numbers, significantly streamlining dispersion engineering for OFC design. We validate our method against experimental data and the results generated with commercial solvers, demonstrating excellent agreement in effective indices, integrated dispersion, and resonance linewidths for silicon nitride resonators excited with lasers operating at 1060 nm and 1550 nm. Our results highlight the solver's utility in predicting anomalous dispersion and coupling dynamics, offering a robust tool for designing high-performance OFC devices.

## Introduction

Optical frequency combs (OFCs) are powerful tools that provide a set of discrete, equally spaced spectral lines, with the potential to revolutionize various fields such as precision spectroscopy [1–4], optical metrology [2, 5], telecommunications [2], and quantum information processing [3, 6]. The ability to generate and control OFCs with high stability and broad bandwidth has enabled the realization of optical clocks [5], frequency synthesis [1], and high-capacity data transmission systems [2]. Among various platforms for OFC generation, microresonator-based frequency combs—also known as Kerr combs, as illustrated in Fig. 1—have attracted significant attention due to their compact size, high  $Q$ -factors, and compatibility with photonic integration [2, 7–10].

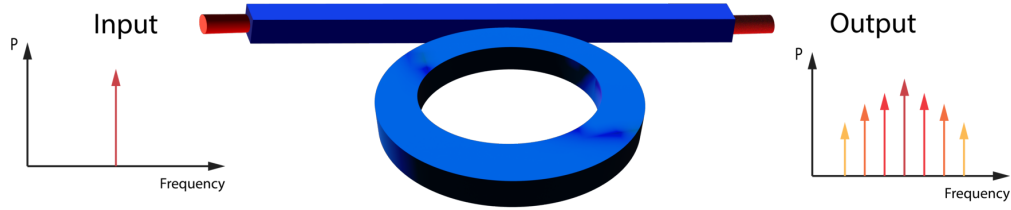


**Figure 1:** Schematic illustration of optical frequency comb generation via bus waveguide coupled to a dielectric ring resonator. A continuous-wave (single-frequency) laser is launched into a bus waveguide (left), which is side-coupled to a dielectric ring resonator. Nonlinear interactions within the resonator lead to the generation of equidistant spectral lines, forming a frequency comb.

Designing resonator geometries that support broadband and low-noise frequency combs requires precise dispersion engineering, which in turn depends on accurate and efficient numerical simulation tools. Sev-

eral numerical methods are available to model electromagnetic wave propagation in dielectric resonators, including time-domain techniques such as the finite-difference time-domain (FDTD) method [11, 12], and frequency-domain methods such as the finite element method (FEM) [13–16], mode matching [17], and the finite-difference frequency-domain (FDFD) method [18–24]. Among these, FDTD is a general-purpose solver capable of modeling complex time-domain phenomena, including nonlinear frequency comb dynamics. However, for large-scale or high- $Q$  resonators, its computational cost becomes prohibitive due to the need for fine spatial and temporal resolution over long simulation windows. This is why the most common method for analyzing optical frequency comb generation is typically handled in two steps. First, modal analysis is performed using numerical solvers such as the finite element method (FEM) or finite differences frequency domain (FDFD) method. These solvers are used to compute the electromagnetic field profiles and the corresponding effective refractive indices of the confined or resonant modes in both the bus waveguide [25] and the dielectric resonator. High accuracy in this step is crucial, as even slight errors in field profiles or indices can result in significant deviations in predicted resonant behavior and coupling dynamics. Second, the interaction between the waveguide and the resonator is analyzed using coupled mode theory (CMT), which enables an approximate yet powerful framework for evaluating coupling efficiency between the structures [8, 26, 27]. From the computed effective indices, we can derive important dispersion-related quantities such as the group index and integrated dispersion, which are essential for understanding the phase-matching conditions and the bandwidth over which efficient comb generation can occur [7–9]. Once the linear modal and coupling characteristics are understood, non-linear dynamics, particularly those that govern soliton formation and frequency comb evolution, are modeled by solving the Lugiato-Lefever equation (LLE) [10, 28–32]. This equation incorporates both Kerr nonlinearity and dispersion, and its solution provides insight into the steady-state and transient behaviors of the system under realistic operating conditions.

Frequency-domain methods offer an attractive alternative for the linear modal analysis stage of design. Among the frequency-domain methods, FEM provides geometric flexibility for modeling irregular or curved waveguide cross-sections, though it requires sophisticated meshing and high-order basis functions. Mode matching divides the waveguide into subregions with known analytical modal solutions and enforces continuity at interfaces. While this approach avoids numerical dispersion errors, it often requires a large number of modes to converge in high-index-contrast structures. The FDFD method offers a favorable tradeoff between simplicity and accuracy. It uses structured grids to discretize Maxwell’s equations directly, making it especially well-suited for exploratory design and research applications. Existing FDFD methods for axially symmetric structures typically operate either in cylindrical coordinates [19] or transformed Cartesian grids [18, 20–24, 33]. They usually solve for two transverse components of either the electric field ( $\mathbf{E}$ ) [19, 22] or magnetic field ( $\mathbf{H}$ ) [21, 23, 24], with the remaining components inferred numerically. However, because resonant modes in dielectric rings are hybrid—lacking pure transverse-electric (TE) or transverse-magnetic (TM) character—field-only formulations may produce spurious modes. Solving for both  $\mathbf{E}$  and  $\mathbf{H}$  concurrently improves reliability by avoiding these artifacts.

In this work, we present a new formulation for electromagnetic wave propagation in dielectric rings and implement it in MATLAB using a finite-differences approach. Our solver enables rapid and accurate modal analysis in ring geometries, making it well-suited for exploring the dispersion characteristics essential for designing structures for optical frequency comb generation. As a first application, we investigated a dielectric ring resonator exhibiting anomalous dispersion near 1060 nm and successfully verified our numerical results against experimental data reported in a recent publication [9]. Subsequently, we applied our solver to study frequency comb generation near 1550 nm. The numerically obtained free spectral range (FSR) and full-width at half-maximum (FWHM) values show strong agreement with our experimental measurements, confirming the accuracy and utility of our method for frequency comb-related applications.

The importance of this work can be summarized as follows.

- Unlike some previous studies [19], our formulation accounts for the non-zero divergence of the electric field at material boundaries, ensuring more accurate field solutions.
- Unlike some earlier work [21, 23, 24], we derive the formulation in cylindrical coordinates; hence, we do not use the coordinate transformation approximation.
- Unlike it is done in earlier studies [33], our method does not neglect the field components in the direction of propagation, enabling a complete description of hybrid modes in dielectric resonators.
- Our solver concurrently computes the  $\mathbf{E}$  and  $\mathbf{H}$  fields, eliminating spurious modes and improving reliability.

- We rigorously benchmarked our numerical results against experimental data and the ones obtained with commercial solvers, COMSOL Multiphysics and Tidy3D.

## Results

Figure 2 illustrates a dielectric ring with a central radius of  $R_c$ , width of  $w_r$ , and height of  $h_r$ . The background does not have to be a homogeneous medium. The ring can be placed on a substrate, for example, as illustrated in Fig. 2. The only requirement regarding the background is that it has to have cylindrical symmetry with respect to the  $z$ -axis. So, the relative permittivity ( $\varepsilon$ ) is a function of  $\rho$  and  $z$ . We assume the entire structure is non-magnetic, i.e.,  $\mu(\rho, z) = \mu_0$ , where  $\mu_0$  is the magnetic permeability of free space.

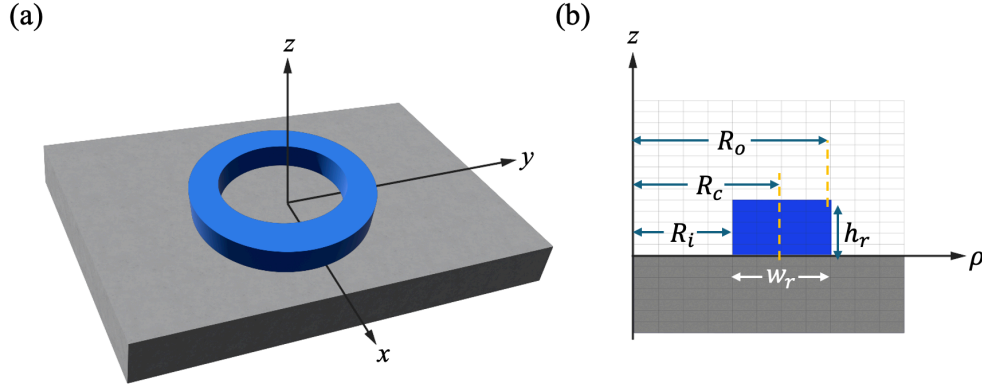


**Figure 2:** A dielectric ring with a width of  $w_r$ , a height of  $h_r$ , and a central radius of  $R_c$  on a substrate: (a) three-dimensional and (b) two-dimensional views.  $R_i$  and  $R_o$  are the inner and outer radii of the ring, i.e.,  $R_i = R_c - w_r/2 = R_o - w_r$ . By assuming the material properties are uniform axially around the  $z$ -axis, the problem can be solved in two dimensions using differential vector operators in the cylindrical coordinate system.

We discretize the computational domain along a rectangular grid by selecting  $N_\rho$  uniformly distributed samples along the  $\rho$ -direction and  $N_z$  uniformly distributed samples along the  $z$ -direction as shown in Fig. 2 (b). We compute the first- and second-order derivatives using central finite differences [25]. We place a perfectly matched layer around the boundary following the recipe developed by Berenger [34]. As explained on page 36 of Kogelnik’s pioneering work [35], the fields outside the dielectric waveguides decay exponentially for the guided modes. Hence, placing the ring at the center of a computational domain that is  $(w_r + \lambda) \times (h_r + \lambda)$ , where  $w_r$  and  $h_r$  are the ring width and height, is sufficient to obtain accurate results to determine the resonant modes of a ring surrounded by a homogeneous background. However, if a thin film and/or substrate are present, the computational domain should be enlarged to adequately capture their effect on wave propagation.

## Integrated Dispersion Study

For the first example, we carry out modal analysis on the dielectric ring studied in a recent study [9]. The ring’s outer radius, width, and height are  $23 \mu\text{m}$ ,  $890 \text{ nm}$ , and  $670 \text{ nm}$ , respectively. The ring is made from silicon nitride [4] (SiN) and surrounded by silicon dioxide [36] ( $\text{SiO}_2$ ). For the numerical solution, we use a  $160 \times 120$  grid on the  $\rho - z$  plane with a 35-point-per-wavelength sampling density.

The first three columns of Fig. 3 show the magnitude of the electric (first row) and magnetic (second row) fields’  $\rho$ ,  $\phi$ , and  $z$  components on the  $\rho - z$  plane for the first resonant mode obtained with our solver. In the last column, we provide field profile examples ( $|E_z|$  and  $|H_z|$ ) obtained with COMSOL. These solutions demonstrate a close agreement, with only minor deviations within acceptable numerical tolerance levels. We observe that the electric field is well-confined within the high-index SiN region, with some fields extending slightly outside the boundaries due to the evanescent field. The symmetry of the fields is consistent with the fundamental resonant mode, where fields are strongly coupled to the geometry of the ring.

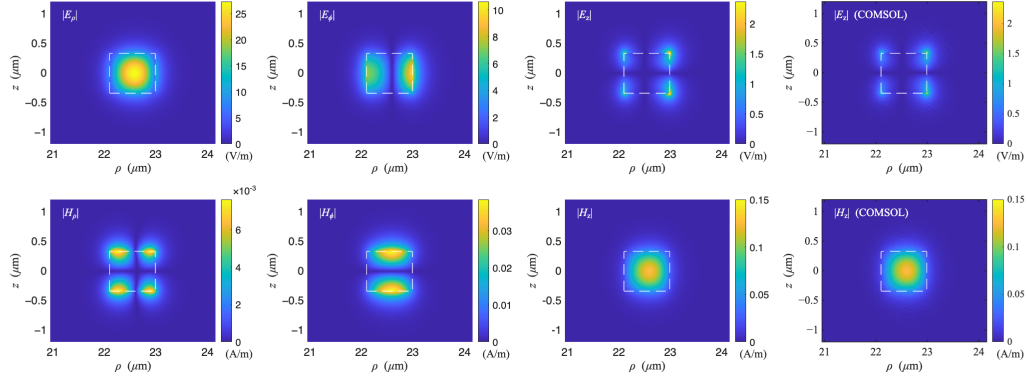


**Figure 3:** Left three columns: magnitude of the electric (top row) and magnetic (bottom row) fields'  $\rho$ ,  $\phi$ , and  $z$  components for the first resonant mode of the electromagnetic waves computed with our solver. The last column shows  $|E_z|$  and  $|H_z|$  distributions obtained with COMSOL. The white dashed lines outline the boundaries of the ring, giving insight into how the electromagnetic fields are confined but not completely symmetric.

The results presented in Table 1 demonstrate excellent agreement between our solver and two widely used commercial solvers—COMSOL Multiphysics and Tidy3D—for the effective refractive indices of the first eight resonant modes. For all modes, the effective indices computed by our method closely match those obtained from COMSOL and Tidy3D, with discrepancies typically on the order of  $10^{-4}$  or less.

**Table 1:** Effective refractive indices of the first four resonant modes of a SiN ring buried in SiO<sub>2</sub>, computed with COMSOL, Tidy3D, and our solver.

mode index	$n_{\text{eff}}$ (COMSOL)	$n_{\text{eff}}$ (Tidy3D)	$n_{\text{eff}}$ (This work)
1	1.8688	1.8688	1.8684
2	1.8567	1.8563	1.8563
3	1.6834	1.6831	1.6831
4	1.6642	1.6643	1.6641
5	1.6077	1.6079	1.6074
6	1.5543	1.5539	1.5541
7	1.5229	1.5533	1.5227
8	1.4908	1.4922	1.4907

In conventional electromagnetic solvers such as ANSYS Lumerical and COMSOL Multiphysics, modal analysis of dielectric ring resonators requires an initial guess for the effective index (in ANSYS Lumerical) or azimuthal mode number (in COMSOL Multiphysics), which is approximately given by  $\beta R_c$ , where  $\beta$  is the unknown propagation constant. After finding one mode, users iteratively try neighboring integers to locate additional resonant modes. This trial-and-error process can be cumbersome and time-consuming. In contrast, our mathematical formulation eliminates the need for such manual input. By specifying only the number of desired modes, our solver automatically computes the corresponding field distributions and effective indices. As illustrated in Fig. 4, we efficiently obtained the effective indices of the first 40 modes in just four minutes on a standard 2021 Apple MacBook Pro with 32 GB of RAM, averaging 6 seconds per mode. This performance is comparable to COMSOL's computation time using a high-quality mesh of 30 points per wavelength, but without the burden of manual parameter tuning, providing a more streamlined and scalable approach to dielectric ring resonator analysis.

To characterize the dispersive properties of the dielectric ring resonator, we first compute the frequency-dependent effective refractive index,  $n_{\text{eff}}$ , using the proposed numerical formulation. The calculations are performed at 100 evenly spaced frequency points ranging from 200 THz to 350 THz. The resulting effective index profile is shown in Fig. 5(a). From the effective index data, we derive the group index using the relation  $n_g = n_{\text{eff}} - \lambda dn_{\text{eff}}/d\lambda$ , where  $\lambda$  is the corresponding wavelength. The computed group index is presented in Fig. 5(b). Next, we calculate the integrated dispersion, defined as the deviation of the resonant

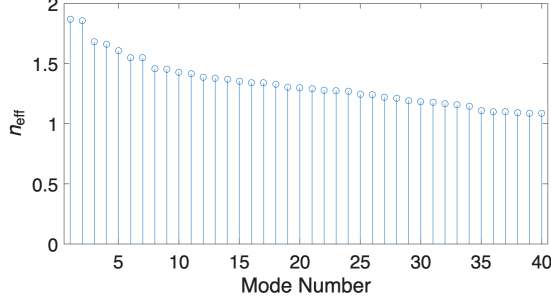


**Figure 4:** The effective index of the first 40 modes computed with our solver.

frequencies from a perfectly equidistant grid:  $D_{\text{int}}(\mu) = \omega_\mu - (\omega_0 + D_1\mu)$ , where  $\omega_\mu$  denotes the angular frequency of the  $\mu^{\text{th}}$  resonant mode,  $\omega_0$  is the pump frequency (set to 283 THz, corresponding to 1060 nm), and  $D_1$  is the free spectral range (FSR) at the pump frequency in rad/s. The calculation of  $D_{\text{int}}$  is essential, as it enables us to identify the anomalous dispersion regime, a necessary condition for soliton formation in microresonator-based optical frequency combs. The computed integrated dispersion is shown in Fig. 5(c). Our numerical results (blue line) exhibit a good agreement with the experimental data [9], which are overlaid as red circular markers.

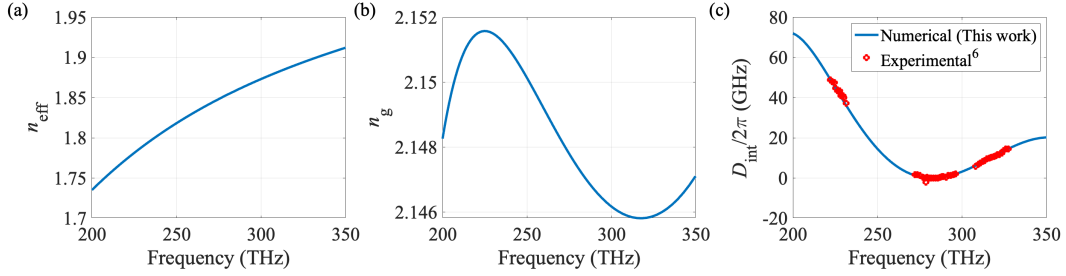


**Figure 5:** (a) Effective refractive index  $n_{\text{eff}}$  as a function of frequency, computed using our numerical formulation. (b) Corresponding group index  $n_g$  derived from the wavelength dependence of  $n_{\text{eff}}$ . (c) Integrated dispersion  $D_{\text{int}}/2\pi$  in GHz compared with experimental measurements from Ref. [3]. The pump frequency is 283 THz (1060 nm).

## Frequency Comb Generation Study

We investigate the frequency comb generation both experimentally and numerically, utilizing a high- $Q$  microresonator based on a silicon nitride ( $\text{Si}_3\text{N}_4$ ) ring, again surrounded with  $\text{SiO}_2$ . The central radius of the ring resonator is  $R_c = 225 \mu\text{m}$ , with a ring width of  $w_r = 1.55 \mu\text{m}$  and a height of  $h_r = 0.8 \mu\text{m}$ . The bus waveguide, which couples light into the resonator, has identical cross-sectional dimensions ( $1.55 \mu\text{m} \times 0.8 \mu\text{m}$ ). The gap between the waveguide and ring is  $g = 0.5 \mu\text{m}$ . The excitation wavelength is  $1.55 \mu\text{m}$ .

For the numerical solution, we use a 200 by 80 grid with a 25 nm mesh length along the horizontal and vertical axes. The propagation loss is assumed to be  $\alpha = 0.06 \text{ dB/cm}$ . The effective index is computed to be 1.8436. Since the ring's radius is very large compared to the  $\lambda$ , the effective index of the first resonant mode is 1.8448, very close to the effective index of the waveguide. The group index is determined to be 2.1292, corresponding to an expected FSR of 99.6 GHz based on this approximate formula:  $\text{FSR}_{\text{approx}} \approx c_0/2\pi n_g R_c$ . Figure 6 (a) shows the transmission spectrum obtained with the numerical solution of the power transmission formula [26]. The spectral difference between the two dips, in other words, the FSR, is determined to be 99.6 GHz, which agrees with the approximate number aforementioned before.

Figure 6 (b) presents a detailed view of the resonance observed in both our numerical simulations and experimental measurements. To validate these simulations experimentally, we employed a setup with a primary pump laser operating with low power at 1550.183 nm to characterize the resonator's linewidth.

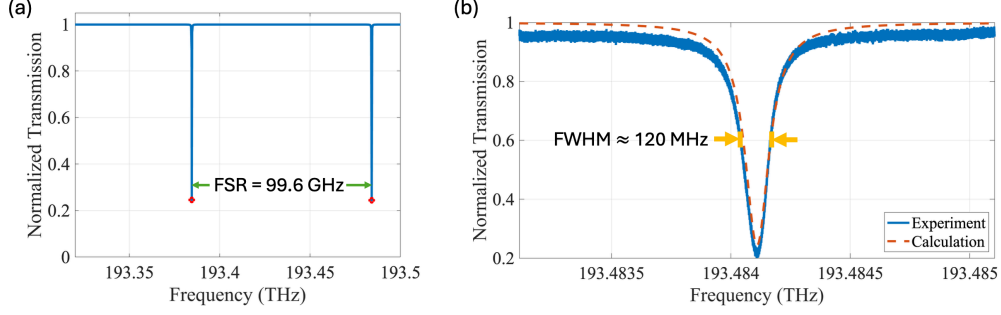


**Figure 6:** (a) Normalized transmission vs. excitation frequency obtained with the numerical solution. (b) A comparison of experimental (blue) and calculated (red) transmission spectra near the resonance.

Both results exhibit a Lorentzian shape with a linewidth (full width at half maximum) of 120 MHz. This narrow linewidth corresponds to a high quality factor ( $Q$ -factor = pump frequency/ $\Delta_{\text{FWHM}}$ ) of 1.6 million, indicating a highly confined resonance. It is important to note that this  $Q$ -factor represents the total or loaded quality factor, defined as  $1/Q = 1/Q_c + 1/Q_i$ , and is distinct from the coupling quality factor ( $Q_c$ ) and the intrinsic resonance quality ( $Q_i$ ) of the ring. The average coupling quality factor, which characterizes the energy transfer efficiency between the waveguide and the ring, was numerically determined to be 2.2 million. The close correspondence between the numerical and experimental results validates the accuracy of our numerical model and confirms the high performance of the device fabricated by Ligentec.

## Methods

### Numerical Model

The electric ( $\mathbf{E}$ ) and magnetic ( $\mathbf{H}$ ) field components of the electromagnetic wave propagating inside the dielectric ring can be represented as sums of three orthogonal vectors as follows

$$\mathbf{E}(\rho, \phi, z) = \left\{ \hat{\rho} E_\rho(\rho, z) + \hat{\phi} E_\phi(\rho, z) + \hat{z} E_z(\rho, z) \right\} e^{-j\nu\phi}, \quad (1)$$

$$\mathbf{H}(\rho, \phi, z) = \left\{ \hat{\rho} H_\rho(\rho, z) + \hat{\phi} H_\phi(\rho, z) + \hat{z} H_z(\rho, z) \right\} e^{-j\nu\phi}, \quad (2)$$

assuming  $e^{-j\nu\phi}$  dependence,  $\nu$  is the angular propagation constant,  $\rho$  is the radial distance from the origin to the point projected onto the  $xy$  plane,  $\phi$  is the azimuthal angle, and  $z$  is the height or vertical distance from the  $xy$  plane. Our goal is to determine the  $\nu$  and to compute the propagating modes ( $\mathbf{E}$  and  $\mathbf{H}$ ) along the  $\phi$  direction inside the dielectric ring for a given frequency ( $f$ ), corresponding to the wavelength  $\lambda = c_0/f$ , where  $c_0$  is the velocity of electromagnetic waves in vacuum.

To carry out modal analysis, we start with Maxwell's equations to derive the Helmholtz wave equations for the electric and magnetic fields in a source-free, lossless, and non-magnetic medium. After expanding each term of the electric field equation, we obtain the following three sets of scalar equations by enforcing each side of the equation to be the same in the  $\hat{\rho}$ ,  $\hat{\phi}$ , and  $\hat{z}$  directions:

$\hat{\rho}$  direction:

$$\left( \mathcal{L} - \frac{1}{R_c^2} + \frac{\rho^2}{R_c^2} \frac{\partial}{\partial \rho} \frac{1}{\varepsilon} \frac{\partial \varepsilon}{\partial \rho} \right) E_\rho + \frac{2j\beta}{R_c} E_\phi + \frac{\rho^2}{R_c^2} \frac{\partial}{\partial \rho} \frac{1}{\varepsilon} \frac{\partial \varepsilon}{\partial z} E_z = \beta^2 E_\rho, \quad (3)$$

$\hat{\phi}$  direction:

$$\left( -\frac{2j\beta}{R_c} - \frac{j\beta\rho}{R_c\varepsilon} \frac{\partial \varepsilon}{\partial \rho} \right) E_\rho + \left( \mathcal{L} - \frac{1}{R_c^2} \right) E_\phi - \frac{j\beta\rho}{R_c\varepsilon} \frac{\partial \varepsilon}{\partial z} E_z = \beta^2 E_\phi, \quad (4)$$

$\hat{z}$  direction:

$$\frac{\rho^2}{R_c^2} \frac{\partial}{\partial z} \frac{1}{\varepsilon} \frac{\partial \varepsilon}{\partial \rho} E_\rho + \mathcal{L} E_z + \frac{\rho^2}{R_c^2} \frac{\partial}{\partial z} \frac{1}{\varepsilon} \frac{\partial \varepsilon}{\partial z} E_z = \beta^2 E_z, \quad (5)$$

where

$$\mathcal{L} = \frac{\rho^2}{R_c^2} \left( \frac{\partial^2}{\partial \rho^2} + \frac{1}{\rho} \frac{\partial}{\partial \rho} + \frac{\partial^2}{\partial z^2} + k_0^2 \epsilon_r \right). \quad (6)$$

Following a similar procedure on the Helmholtz wave equation for the magnetic field, we obtain three other equations. However, since we will only need the one along the  $\hat{z}$  direction, we provide it below for the sake of completeness.

$$\frac{\rho^2}{R_c^2} \frac{1}{\epsilon} \frac{\partial \epsilon}{\partial \rho} \frac{\partial H_\rho}{\partial z} + \left( \mathcal{L} - \frac{\rho^2}{R_c^2} \frac{1}{\epsilon} \frac{\partial \epsilon}{\partial \rho} \frac{\partial}{\partial \rho} \right) H_z = \beta^2 H_z. \quad (7)$$

It is known that mixed electric field–magnetic field formulations allow for direct enforcement of boundary conditions on both electric and magnetic fields at interfaces between materials [16]. In single-field formulations, deriving the secondary field (electric from magnetic or vice versa) often complicates boundary condition enforcement, introducing errors at material interfaces [25]. From Maxwell's equations, one can derive the following expressions:

$$E_\phi = \frac{1}{j\omega\epsilon} \left( \frac{\partial H_\rho}{\partial z} - \frac{\partial H_z}{\partial \rho} \right), \quad (8) \quad H_\phi = \frac{1}{j\omega\mu_0} \left( \frac{\partial E_z}{\partial \rho} - \frac{\partial E_\rho}{\partial z} \right). \quad (9)$$

By using Eq. (8), we rewrite Eq. (3) in the following form

$$\left( \mathcal{L} - \frac{1}{R_c^2} + \frac{\rho^2}{R_c^2} \frac{\partial}{\partial \rho} \frac{1}{\epsilon} \frac{\partial \epsilon}{\partial \rho} \right) E_\rho + \left( \frac{\rho^2}{R_c^2} \frac{\partial}{\partial \rho} \frac{1}{\epsilon} \frac{\partial \epsilon}{\partial z} \right) E_z + \frac{2\beta}{\omega\epsilon R_c} \left( \frac{\partial H_\rho}{\partial z} - \frac{\partial H_z}{\partial \rho} \right) = \beta^2 E_\rho. \quad (10)$$

Similarly,  $\hat{\rho}$  component of the  $H$ -formulation becomes

$$\left( \mathcal{L} - \frac{\rho^2}{R_c^2} \frac{1}{\epsilon} \frac{\partial \epsilon}{\partial z} \frac{\partial}{\partial z} - \frac{1}{R_c^2} \right) H_\rho + \frac{\rho^2}{R_c^2} \frac{1}{\epsilon} \frac{\partial \epsilon}{\partial z} \frac{\partial}{\partial z} H_z + \frac{2\beta}{\omega\mu_0 R_c} \left( \frac{\partial E_z}{\partial \rho} - \frac{\partial E_\rho}{\partial z} \right) = \beta^2 H_\rho. \quad (11)$$

Eqs. (10), (11), (5), and (7) can be cast into a matrix equation such as

$$\overline{\overline{M}}\mathbf{E} + \beta\overline{\overline{L}}\mathbf{E} - \beta^2\overline{\overline{I}}\mathbf{E} = 0, \quad (12)$$

where  $\overline{\overline{M}}$  is the matrix independent of  $\beta$ ,  $\overline{\overline{L}}$  is the linear term in  $\beta$ , and the last term is the quadratic term in  $\beta$ .

$$\overline{\overline{M}} = \begin{bmatrix} M_1 & M_2 & 0 & 0 \\ M_3 & M_4 & 0 & 0 \\ 0 & 0 & M_5 & M_6 \\ 0 & 0 & M_7 & M_7 \end{bmatrix} \quad (13)$$

$$\overline{\overline{L}} = \begin{bmatrix} 0 & 0 & L_1 & L_2 \\ 0 & 0 & 0 & 0 \\ L_3 & L_4 & 0 & 0 \\ 0 & 0 & 0 & 0 \end{bmatrix} \quad (14)$$

$$M_1 = \mathcal{L} - \frac{1}{R_c^2} + \frac{\rho^2}{R_c^2} \frac{\partial}{\partial \rho} \frac{1}{\epsilon} \frac{\partial \epsilon}{\partial \rho} \quad (15)$$

$$M_5 = \mathcal{L} - \frac{\rho^2}{R_c^2} \frac{1}{\epsilon} \frac{\partial \epsilon}{\partial z} \frac{\partial}{\partial z} - \frac{1}{R_c^2} \quad (19)$$

$$M_2 = \frac{\rho^2}{R_c^2} \frac{\partial}{\partial \rho} \frac{1}{\epsilon} \frac{\partial \epsilon}{\partial z} \quad (16)$$

$$M_6 = \frac{\rho^2}{R_c^2} \frac{1}{\epsilon} \frac{\partial \epsilon}{\partial z} \frac{\partial}{\partial z} \quad (20)$$

$$M_3 = \frac{\rho^2}{R_c^2} \frac{\partial}{\partial z} \frac{1}{\epsilon} \frac{\partial \epsilon}{\partial \rho} \quad (17)$$

$$M_7 = \frac{\rho^2}{R_c^2} \frac{1}{\epsilon} \frac{\partial \epsilon}{\partial \rho} \frac{\partial}{\partial z} \quad (21)$$

$$M_4 = \mathcal{L} + \frac{\rho^2}{R_c^2} \frac{\partial}{\partial z} \frac{1}{\epsilon} \frac{\partial \epsilon}{\partial z} \quad (18)$$

$$M_8 = \mathcal{L} - \frac{\rho^2}{R_c^2} \frac{1}{\epsilon} \frac{\partial \epsilon}{\partial \rho} \frac{\partial}{\partial \rho} \quad (22)$$

$$L_1 = \frac{2m}{\omega\epsilon R_c^2} \frac{\partial H_\rho}{\partial z} \quad (23)$$

$$L_3 = -\frac{2m}{\omega\mu_0 R_c^2} \frac{\partial}{\partial z} \quad (25)$$

$$L_2 = -\frac{2m}{\omega\epsilon R_c^2} \frac{\partial H_z}{\partial \rho} \quad (24)$$

$$L_4 = \frac{2m}{\omega\mu_0 R_c^2} \frac{\partial}{\partial \rho} \quad (26)$$

This can be rewritten as a linear generalized eigenvalue problem by introducing an auxiliary variable  $\mathbf{F} = \beta\mathbf{E}$ , leading to  $\overline{\overline{M}}\mathbf{E} + \overline{\overline{L}}\mathbf{F} - \mathbf{F}\beta = 0$ , which gives the augmented system:

$$\begin{pmatrix} \overline{\overline{M}} & \overline{\overline{L}} \\ 0 & \overline{\overline{I}} \end{pmatrix} \begin{pmatrix} \mathbf{E} \\ \mathbf{F} \end{pmatrix} = \beta \begin{pmatrix} 0 & \overline{\overline{I}} \\ \overline{\overline{I}} & 0 \end{pmatrix} \begin{pmatrix} \mathbf{E} \\ \mathbf{F} \end{pmatrix}. \quad (27)$$

We solve this linear generalized eigenvalue problem using MATLAB’s `eigs` function, which is optimized for large sparse matrices. After solving, we retain only the physically meaningful modes (those with  $n_{\text{eff}}^{\text{ring}} < n_{\text{ring}}$ , where  $n_{\text{eff}}^{\text{ring}} = \beta/k_0$  is the effective index of the ring and  $n_{\text{ring}}$  is the refractive index of the material which ring is made from.)

## Experiment Setup

Figure 7 illustrates the experimental configuration used to study the dynamics of frequency comb generation in a dielectric waveguide coupled to a dielectric ring resonator. A primary pump laser initiates the generation of soliton frequency combs by leveraging nonlinear effects like Kerr nonlinearity and four-wave mixing within this system. To enhance stability and widen the operational range for solitons, an auxiliary laser is employed to regulate resonator power. Each laser source is protected from back reflections by optical isolators positioned at their outputs. The pump light’s intensity is increased by an erbium-doped fiber amplifier (EDFA) before being coupled into the microresonator using a circulator. A second circulator performs two roles: it directs the output light to various measurement devices and allows the auxiliary laser to enter the resonator propagating counter to the primary pump. The optical output is converted to electrical signals by two photodetectors, enabling time-domain analysis of the pulse train with an oscilloscope. Simultaneously, an optical spectrum analyzer measures the spectral features of the generated frequency comb.

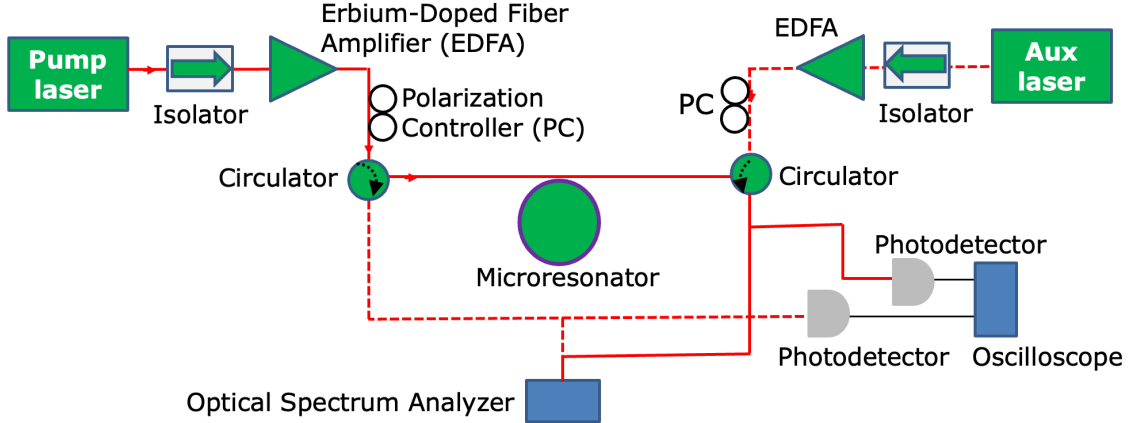


**Figure 7:** Schematic of the experimental setup for frequency comb generation and analysis. The red solid lines indicate the primary laser path for soliton frequency comb generation, while the red dashed lines represent the auxiliary laser used to compensate for the resonator’s thermal shift. The output is analyzed using photodetectors, an oscilloscope, and an optical spectrum analyzer.

## Discussions

Our numerical method is highly accurate for simple geometries like rectangles and circles in the  $\rho$ - $z$  plane, where 20 points per wavelength (PPW) is sufficient. Complex shapes require higher densities; we recommend starting at 20 PPW and increasing by 5 PPW until eigenvalues converge. For non-rectangular cross-sections (e.g., trapezoids in the  $\rho$  -  $z$  plane), a rectangular mesh causes geometric inaccuracies (“stair-step” effect), impacting boundary precision, the effective refractive index, and is especially problematic for higher-order azimuthal modes, potentially causing spurious effects. While higher resolution helps, advanced techniques like FEM, possibly with radiation boundary conditions [15], offer better accuracy.



## Conclusion

In this work, we presented a novel finite-difference frequency-domain formulation for electromagnetic modal analysis in dielectric ring resonators, addressing key limitations of existing methods. Our approach solves for both electric and magnetic fields simultaneously in cylindrical coordinates, eliminating spurious modes and ensuring accurate field solutions—particularly at material boundaries where earlier formulations failed. By avoiding coordinate transformations and retaining all field components, our method provides a complete description of hybrid modes, crucial for modeling microresonators used in optical frequency comb generation. We validated our solver through rigorous benchmarks against COMSOL Multiphysics, Tidy3D, and experimental data, demonstrating excellent agreement in effective refractive indices, dispersion profiles, and resonance characteristics. Notably, our method automates mode computation without requiring manual input for azimuthal mode numbers, significantly streamlining the design process. Applied to SiN ring resonators, our solver accurately predicted anomalous dispersion near 1060 nm and reproduced experimental free spectral ranges and linewidths at 1550 nm, confirming its utility for Kerr frequency comb design.

## Acknowledgments

This work has been supported in part by cooperative agreements with the National Center for Manufacturing Sciences 2022138-142232 and 2023200-142386, which are sub-contracts from the US-DoD cooperative agreements HQ0034-20-2-0007 and HQ0034-24-2-0001, respectively. The authors acknowledge useful discussions with J. P. Cahill, T. Mahmood, and W. Zhou of the Army Research Laboratory and G. Moille and K. Srinivasan of NIST and UMD-JQI.

## Author contributions statement

E.S. developed the formulation and implemented it in MATLAB. A.N. and G.M.C. built the experiment setup and conducted the measurements. R.I. and L.C. carried out numerical simulations. E.S. and C.R.M. wrote the first draft of the manuscript. All authors worked together on the final version of the manuscript.

## Data availability

The code to reproduce the results provided in this manuscript can be found at <https://github.com/simsekergun/DieRingSolver> [37].

## References

- [1] R. Holzwarth, T. Udem, T. W. Hänsch, J. C. Knight, W. J. Wadsworth, and P. S. J. Russell, “Optical frequency synthesizer for precision spectroscopy,” *Phys. Rev. Lett.*, vol. 85, pp. 2264–2267, Sep 2000.
- [2] T. J. Kippenberg, R. Holzwarth, and S. A. Diddams, “Microresonator-based optical frequency combs,” *Science*, vol. 332, no. 6029, pp. 555–559, 2011.
- [3] N. Picqué and T. W. Hänsch, “Frequency comb spectroscopy,” *Nature Photonics*, vol. 13, no. 3, pp. 146–157, 2019.
- [4] K. Luke, Y. Okawachi, M. R. E. Lamont, A. L. Gaeta, and M. Lipson, “Broadband mid-infrared frequency comb generation in a si<sub>3</sub>n<sub>4</sub> microresonator,” *Opt. Lett.*, vol. 40, pp. 4823–4826, Nov 2015.
- [5] T. Udem, R. Holzwarth, and T. W. Hänsch, “Optical frequency metrology,” *Nature*, vol. 416, no. 6877, pp. 233–237, 2002.
- [6] M. Kues, C. Reimer, J. M. Lukens, W. J. Munro, A. M. Weiner, D. J. Moss, and R. Morandotti, “Quantum optical microcombs,” *Nature Photonics*, vol. 13, no. 3, pp. 170–179, 2019.

- [7] T. Herr, K. Hartinger, J. Riemensberger, C. Y. Wang, E. Gavartin, R. Holzwarth, M. L. Gorodetsky, and T. J. Kippenberg, “Universal formation dynamics and noise of Kerr-frequency combs in microresonators,” *Nature Photonics*, vol. 6, no. 7, pp. 480–487, 2012.
- [8] G. Moille, Q. Li, T. C. Briles, S.-P. Yu, T. Drake, X. Lu, A. Rao, D. Westly, S. B. Papp, and K. Srinivasan, “Broadband resonator-waveguide coupling for efficient extraction of octave-spanning microcombs,” *Optics Letters*, vol. 44, no. 19, pp. 4737–4740, 2019.
- [9] G. Moille, P. Shandilya, A. Niang, C. Menyuk, G. Carter, and K. Srinivasan, “Versatile optical frequency division with kerr-induced synchronization at tunable microcomb synthetic dispersive waves,” *Nature Photonics*, vol. 19, no. 1, pp. 36–43, 2025.
- [10] Y. K. Chembo, “Kerr optical frequency combs: Theory, applications and perspectives,” *Nanophotonics*, vol. 5, no. 2, pp. 214–230, 2016.
- [11] A. Taflov and S. C. Hagness, *Computational Electrodynamics: The Finite-Difference Time-Domain Method*, ch. 16. Artech House, 3rd ed., 2005.
- [12] B. M. A. Rahman, D. M. H. Leung, S. S. A. Obayya, and K. T. V. Grattan, “Numerical analysis of bent waveguides: bending loss, transmission loss, mode coupling, and polarization coupling,” *Appl. Opt.*, vol. 47, pp. 2961–2970, Jun 2008.
- [13] J.-M. Jin, *The finite element method in electromagnetics*, ch. 7. Wiley-IEEE, 2002.
- [14] K. Kakiyama, N. Kono, K. Saitoh, and M. Koshida, “Full-vectorial finite element method in a cylindrical coordinate system for loss analysis of photonic wire bends,” *Optics Express*, vol. 14, no. 23, pp. 11128–11141, 2006.
- [15] E. Simsek, J. Liu, and Q. Liu, “A spectral integral method and hybrid SIM/FEM for layered media,” *IEEE Transactions on Microwave Theory and Techniques*, vol. 54, no. 11, pp. 3878–3884, 2006.
- [16] B. M. Notaros, “Higher order frequency-domain computational electromagnetics,” *IEEE Transactions on Antennas and Propagation*, vol. 56, no. 8, pp. 2251–2276, 2008.
- [17] L. Prkna, M. Hubalek, and J. Ctyroky, “Vectorial eigenmode solver for bent waveguides based on mode matching,” *IEEE Photonics Technology Letters*, vol. 16, no. 9, pp. 2057–2059, 2004.
- [18] W. Pascher and R. Pregla, “Vectorial analysis of bends in optical strip waveguides by the method of lines,” *Radio Science*, vol. 28, no. 6, pp. 1229–1233, 1993.
- [19] S. Kim and A. Gopinath, “Vector analysis of optical dielectric waveguide bends using finite-difference method,” *Journal of Lightwave Technology*, vol. 14, no. 9, pp. 2085–2092, 1996.
- [20] J. Xiao, H. Ni, and X. Sun, “Full-vector mode solver for bending waveguides based on the finite-difference frequency-domain method in cylindrical coordinate systems,” *Optics Letters*, vol. 33, no. 16, pp. 1848–1850, 2008.
- [21] J. Xiao, H. Ma, N. Bai, X. Liu, and X. Sun, “Full-vectorial analysis of bending waveguides using finite difference method based on H-fields in cylindrical coordinate systems,” *Optics Communications*, vol. 282, no. 13, pp. 2511–2515, 2009.
- [22] J. Xiao and X. Sun, “Full-vector analysis of optical dielectric waveguide bends using improved finite difference method based on E fields in cylindrical coordinate systems,” *Journal of Optics*, vol. 12, no. 5, p. 055404, 2010.
- [23] J. Xiao and X. Sun, “Vector analysis of bending waveguides by using a modified finite-difference method in a local cylindrical coordinate system,” *Optics Express*, vol. 20, no. 19, pp. 21583–21597, 2012.
- [24] X. Wu and J. Xiao, “Full-vector analysis of bending waveguides by using meshless finite cloud method in a local cylindrical coordinate system,” *Journal of Lightwave Technology*, vol. 39, no. 22, pp. 7199–7209, 2021.

- [25] E. Simsek, “Practical vectorial mode solver for dielectric waveguides based on finite differences,” *Opt. Lett.*, vol. 50, pp. 4102–4105, Jun 2025.
- [26] A. Yariv, “Critical coupling and its control in optical waveguide-ring resonator systems,” *IEEE Photonics Technology Letters*, vol. 14, no. 4, pp. 483–485, 2002.
- [27] M. Hammer, K. R. Hiremath, and R. Stoffer, “Analytical approaches to the description of optical microresonator devices,” *AIP Conference Proceedings*, vol. 709, pp. 48–71, 05 2004.
- [28] L. A. Lugiato and R. Lefever, “Spatial dissipative structures in passive optical systems,” *Physical Review Letters*, vol. 58, no. 21, p. 2209, 1987.
- [29] Y. K. Chembo and N. Yu, “Modal expansion approach to optical-frequency-comb generation with monolithic whispering-gallery-mode resonators,” *Phys. Rev. A*, vol. 82, p. 033801, Sep 2010.
- [30] Y. K. Chembo and C. R. Menyuk, “Spatiotemporal lugiato-lefever formalism for kerr-comb generation in whispering-gallery-mode resonators,” *Physical Review A*, vol. 87, no. 5, p. 053852, 2013.
- [31] F. Castelli, M. Brambilla, A. Gatti, F. Prati, and L. A. Lugiato, “The LLE, pattern formation and a novel coherent source,” *The European Physical Journal D*, vol. 71, no. 4, p. 84, 2017.
- [32] D. C. Cole, A. Gatti, S. B. Papp, F. Prati, and L. Lugiato, “Theory of Kerr frequency combs in Fabry-Perot resonators,” *Phys. Rev. A*, vol. 98, p. 013831, Jul 2018.
- [33] W. Lui, C.-L. Xu, T. Hirono, K. Yokoyama, and W.-P. Huang, “Full-vectorial wave propagation in semiconductor optical bending waveguides and equivalent straight waveguide approximations,” *Journal of Lightwave Technology*, vol. 16, no. 5, pp. 910–914, 1998.
- [34] J.-P. Berenger, “A perfectly matched layer for the absorption of electromagnetic waves,” *Journal of Computational Physics*, vol. 114, no. 2, pp. 185–200, 1994.
- [35] H. Kogelnik, “Theory of dielectric waveguides,” in *Integrated optics*, pp. 13–81, Springer, 1975.
- [36] I. H. Malitson, “Interspecimen comparison of the refractive index of fused silica\*,†,” *J. Opt. Soc. Am.*, vol. 55, pp. 1205–1209, Oct 1965.
- [37] E. Simsek, “Dielectric ring solver.” <https://github.com/simsekergun/DieRingSolver/>, 2025.